IOP Publishing Plasma Physics and Controlled Fusion
Plasma Phys. Control. Fusion **60** (2018) 054006 (13pp) https://doi.org/10.1088/1361-6587/aab222

Leveraging extreme laser-driven magnetic fields for gamma-ray generation and pair production

O Jansen[1,2], T Wang[1,2], D J Stark[3], E d'Humières[4], T Toncian[5] and A V Arefiev[1,2]

[1] Department of Mechanical and Aerospace Engineering, University of California at San Diego, La Jolla, CA 92093, United States of America
[2] Center for Energy Research, University of California San Diego, La Jolla, CA 92093, United States of America
[3] Los Alamos National Laboratory, Los Alamos, NM 87545, United States of America
[4] Univ. Bordeaux-CNRS-CEA, Centre Lasers Intenses et Applications, UMR 5107, F-33405 Talence, France
[5] Institute for Radiation Physics, Helmholtz-Zentrum Dresden-Rossendorf e.V., D-01328 Dresden, Germany

E-mail: ojansen@ucsd.edu

Received 26 December 2017, revised 14 February 2018
Accepted for publication 26 February 2018
Published 19 March 2018

Abstract

The ability of an intense laser pulse to propagate in a classically over-critical plasma through the phenomenon of relativistic transparency is shown to facilitate the generation of strong plasma magnetic fields. Particle-in-cell simulations demonstrate that these fields significantly enhance the radiation rates of the laser-irradiated electrons, and furthermore they collimate the emission so that a directed and dense beam of multi-MeV gamma-rays is achievable. This capability can be exploited for electron–positron pair production via the linear Breit–Wheeler process by colliding two such dense beams. Presented simulations show that more than 10^3 pairs can be produced in such a setup, and the directionality of the positrons can be controlled by the angle of incidence between the beams.

Keywords: plasma channel, pair creation, high energy radiation, laser acceleration, relativistic transparency, ultra-high magnetic fields, plasma

(Some figures may appear in colour only in the online journal)

1. Introduction

New laser facilities, such as the extreme light infrastructure [1] or multi-PW Apollon facility [2], are expected to deliver laser pulses of unprecedented intensities [3], making it possible to experimentally access the regime of laser–matter interactions with intensities approaching 10^{23} watt cm^{-2}. This prospect has generated a surge of interest in ultra-short laser–matter interactions because of the potential for fundamental physics research and radiation source applications [4] at these elevated field strengths.

The key features of these interactions at extreme laser intensities are that electron dynamics in the target become ultra-relativistic and that quantum electrodynamic processes become relevant to the electron motion and energy distribution. Effectively, the laser–matter interaction in this case is more precisely a laser-plasma interaction, since the irradiated material becomes ionized long before the laser pulse reaches its peak intensity. The relativistic energies of the electrons in these strong fields result in high radiative rates that play an integral role in altering the electron dynamics [5]; as the laser intensity increases, so does the acceleration experienced by electrons in the irradiated plasma. This increase ultimately causes the classical picture of the emission and electron trajectories to break down, making the inclusion of quantum effects a necessity for the models [6, 7].

Previous work in this area of laser-plasma interactions at extreme intensities has shown that the efficiency of photon emissions can be surprisingly high due to the violent acceleration experienced by electrons in the target [8–11]. This acceleration can be induced not just by the laser pulse, but by plasma fields generated in the interaction as well [12]. In this paper we examine how plasma fields that are driven by the irradiating laser pulse can be leveraged to enhance the rate of photon emissions, specifically showing that a laser pulse of extreme intensity tends to drive a strong plasma magnetic field rather than a strong plasma electric field. This magnetic field stimulates emission by laser-irradiated electrons, causing them to generate a directed and dense beam of multi-MeV gamma-rays.

Multiple applications, including advanced nuclear and radiological detection systems, specifically require dense beams of gamma-rays or can directly benefit from laser-driven gamma-ray sources [13]. Furthermore, these sources have the potential to open up new avenues of fundamental research that have been previously inaccessible in the laboratory. In particular, our understanding of the activity in the early Universe and high-energy astrophysics firmly relies on a so-called linear Breit–Wheeler process [14], in which a collision of two energetic photons creates an electron–positron pair. Even though this process has a significant impact on astrophysical phenomena [15–17], it has not been observed in laboratory conditions. Experiments thus far [18] have instead aimed at harnessing the nonlinear Breit–Wheeler process, which utilizes more than two photons per collision. The difficulty in achieving the linear process stems from a low cross-section and a high energy threshold, which translates into needing a source that can supply dense beams of multi-MeV photons. We show that the laser-driven gamma-ray sources based on strong plasma magnetic fields can resolve this difficulty by delivering such a desired beam of photons. Our simulations indicate that a collision of two gamma-ray beams driven by a laser pulse with parameters similar to that of the Apollon facility in France can produce more than 10^3 electron–positron pairs through the linear Breit–Wheeler process in a single shot even when the interaction region is significantly removed from the gamma-ray sources.

The rest of the paper is organized in the following way. In section 2 we examine the dynamics of a single electron irradiated by a plane electromagnetic wave and estimate the threshold for a plasma magnetic field above which the field significantly influences the photon emission by the electron. The fully self-consistent particle-in-cell (PIC) simulations in section 3 demonstrate that such a field can be achieved in laser-plasma interactions at extreme intensities by employing the effect of relativistically induced transparency. These simulations self-consistently calculate the resulting collimated photon beam by taking into account radiation reaction effects that become important in this regime, and we then use two such beams in section 4 to examine pair-creation via the linear Breit–Wheeler process. Finally, we summarize our findings and provide concluding remarks in section 5.

2. Emission of a single electron

It is known from classical electrodynamics that an electron accelerated by electric, **E**, and magnetic, **B**, fields emits electromagnetic radiation. The emitted power, P, is determined by the acceleration in an instantaneous rest frame. It is convenient to quantify this acceleration using a dimensionless parameter [19, p 194], [20]

$$\eta \equiv \frac{\gamma}{E_S}\sqrt{\left(\mathbf{E}+\frac{1}{c}[\mathbf{v}\times\mathbf{B}]\right)^2-\frac{1}{c^2}(\mathbf{E}\cdot\mathbf{v})^2}\,, \tag{1}$$

where γ and $\mathbf{v}$ are the relativistic factor and velocity of the electron, c is the speed of light, and $E_S \approx 1.3\times10^{18}$ V m^{-1} is the Schwinger limit. The radiated power scales as $P \propto \eta^2$.

It is evident from equation (1) that η, and thus the emission rate, increase with the amplitude of the fields acting on the electron. However, the field configuration and its orientation with respect to the electron velocity play a very important role as well [21]. This becomes particularly apparent when considering an electron irradiated by a plane electromagnetic wave. In what follows, we consider several simple yet insightful examples with an increasing degree of sophistication.

In all of the examples, we consider a plane linearly-polarized electromagnetic wave with wavelength λ propagating along the x-axis. Without any loss of generality, we assume that $\mathbf{E}_{\rm wave} = E\mathbf{e}_y$ and $\mathbf{B}_{\rm wave} = B\mathbf{e}_z$, where $\mathbf{e}_y$ and $\mathbf{e}_z$ are unit vectors. Here we invoke the well-known result that $E = B$ for a wave propagating in the positive direction along the x-axis.

Our first example is an ultra-relativistic electron colliding head-on with the wave without any appreciable transverse motion, such that $\mathbf{v} = -v\mathbf{e}_x$. In this case, the velocity is orthogonal to the electric field and the last term on the right-hand side of equation (1) vanishes. Taking into account that $v/c \approx 1$ and $B = E$, we find from equation (1) that

$$\eta_{\rm counter} \approx 2\gamma\frac{|E|}{E_S}, \tag{2}$$

where $\gamma = 1/\sqrt{1-v^2/c^2}$. This result is what one might expect based on the structure of the expression for the parameter η, where both the field amplitude and the γ-factor enter the numerator. This notably permits considerable enhancement of the emission rate due to the relativistic factor, which we will observe is not the case for alternate orientations.

Let us now consider an ultra-relativistic electron that is co-moving with the wave, so that $\mathbf{v} = v\mathbf{e}_x$. The velocity is again orthogonal to the electric field, so the last term on the right-hand side of equation (1) vanishes. In order to estimate the first term on the right-hand side, one needs to take into account that v is slightly smaller than c. Otherwise, this term would vanish as well. The result that follows from equation (1) shows that the value of η is now greatly reduced:

$$\eta_{\rm co} \approx \frac{1}{2\gamma}\frac{|E|}{E_S}. \tag{3}$$

An important aspect here is that η is inversely proportional to the γ-factor. This is because for a co-moving ultra-relativistic

electron the acceleration induced by the electric field of the wave is strongly compensated by the acceleration induced by the magnetic field of the wave. The reduction of the parameter η indicates that the emitted power is strongly suppressed in this case.

These two examples clearly articulate why colliding relativistic electrons with an intense laser pulse is one of the more promising avenues of generating intense radiation and even of examining the effects of radiation reaction [5, 22, 23]. However, it is worth pointing out that colliding setups typically require two laser pulses, and this severely constrains most facilities' capabilities of employing this technique. An additional laser pulse is needed to accelerate electrons and generate an ultra-relativistic bunch for the collision [23].

In contrast to the colliding setup, the co-propagating setup can be achieved using just a single laser pulse. This is because an intense laser pulse can accelerate an electron in the direction of the pulse propagation through so-called direct laser acceleration. If the normalized laser amplitude, $a_0 \equiv |e|E_0/m_e c\omega$, is large, $a_0 \gg 1$, then the laser field induces relativistic electron motion which in turn leads to preferentially forward acceleration. Here m_e and e are the electron mass and charge, while E_0 and ω are the pulse electric field amplitude and its frequency. However, transverse electron oscillations are essential for this mechanism of acceleration, and our previous estimates neglected such oscillations and the resulting increase of the longitudinal momentum that can be substantial [24–26], essentially implicitly assuming that $a_0 \ll 1$. We thus have to revise the estimates for η by taking transverse oscillations into account.

We now briefly overview the direct laser acceleration mechanism in order to provide the context for the result that will follow. Electron acceleration by an intense laser pulse can be conveniently described using the normalized vector potential **a**. This potential specifies the laser fields,

$$\mathbf{E}_{\text{wave}} = -\frac{m_e c}{|e|}\frac{\partial \mathbf{a}}{\partial t}, \tag{4}$$

$$\mathbf{B}_{\text{wave}} = \frac{m_e c^2}{|e|}\nabla \times \mathbf{a} \tag{5}$$

and in our case it is only a function of a normalized phase

$$\xi \equiv \frac{2\pi}{\lambda}(x - ct), \tag{6}$$

so that $\mathbf{a} = a(\xi)\mathbf{e}_y$. For simplicity, let us assume that the amplitude gradually increases and then remains constant, such that $a(\xi) = a_0 \sin(\xi)$. The momentum components of an initially static electron that is irradiated by such a wave are then prescribed by [26]

$$p_x/m_e c = a^2/2, \tag{7}$$

$$p_y/m_e c = a. \tag{8}$$

We see that in addition to oscillating with the electric field, the electron also moves forward along the propagation direction. The electron motion is strongly relativistic for wave amplitudes $a_0 \gg 1$, and that is why such amplitudes are called relativistic. The γ-factor strongly oscillates at these amplitudes,

$$\gamma = 1 + a^2/2, \tag{9}$$

and the electron motion is predominantly directed forward with an angle to the x-axis that can be estimated as $p_y/p_x \sim 1/a$.

We are now well-equipped to calculate the normalized acceleration η for the electron that undergoes the direct laser acceleration at relativistic wave amplitudes. Taking into account that $B_z = E_y \equiv E$ and that the electron can now have a velocity component along the electric field, we find from equation (1) that

$$\begin{aligned}\eta &= \frac{|E|}{E_S}\sqrt{\left(\gamma - \frac{p_x}{m_e c}\right)^2 + \left(\frac{p_y}{m_e c}\right)^2 - \left(\frac{p_y}{m_e c}\right)^2} \\ &= \frac{|E|}{E_S}\left(\gamma - \frac{p_x}{m_e c}\right),\end{aligned} \tag{10}$$

where we explicitly used the relation $v_{x,y} = p_{x,y}/\gamma m_e c$. The expression assumes nothing about the amplitude of the transverse electron momentum oscillations and it can thus be used to calculate η both for the already considered co-propagating case without the transverse motion and for the electrons accelerated using the direct laser acceleration mechanism. By only assuming that $|p_x| \gg |p_y|$, we find that for an ultrarelativistic electron

$$\gamma - \frac{p_x}{m_e c} \approx \frac{1}{2\gamma}\left(1 + \frac{p_y^2}{m_e^2 c^2}\right). \tag{11}$$

This result directly shows how even a relatively small but relativistic transverse momentum can significantly enhance the value of η. Using the expressions for the electron momentum during the direct laser acceleration (equations (7) and (8)) we now find that

$$\eta = \frac{E}{E_S}\left(\gamma - \frac{p_x}{m_e c}\right) \to \eta_{\text{DLA}} = \frac{E}{E_S}. \tag{12}$$

The significant difference between η_{DLA} and η_{co} given by equation (3) is the consequence of the transverse electron oscillations induced by the wave.

Despite the substantial increase of η, and thus the emission, in the direct laser acceleration regime, compared to the co-propagating case, the emitted power is still significantly lower than in the case where the electron collides with the laser pulse. In order to gain further insight and understand what limits the emission during the direct laser acceleration, we examine a corresponding electron trajectory. Figure 1 provides comprehensive information about an electron accelerated from rest by a laser pulse that is gradually ramped up in amplitude to $a_0 = 100$ by showing both the electric and magnetic fields acting on the electron (after the pulse reaches its peak) as well as the electron η and its relativistic γ-factor. One striking feature is that the electron trajectory has stopping points when the laser fields reach their peak amplitude. It then immediately follows from equation (12) that the parameter η also peaks in the vicinity of the stopping points. At these points, the electron halts its motion and its γ-factor drops. We

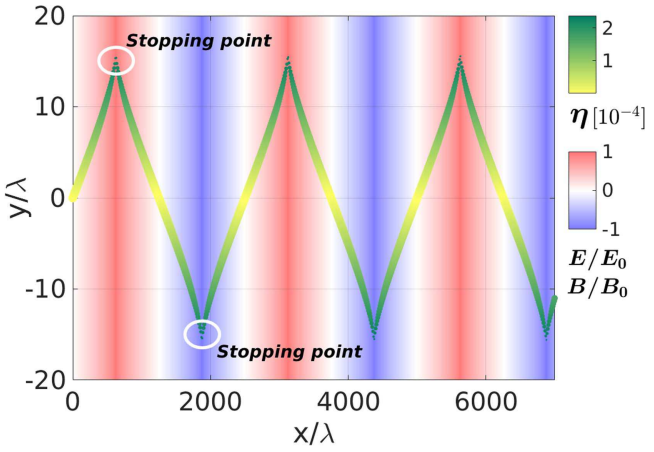

Figure 1. Electron trajectory in a plane wave with a normalized amplitude $a_0 = 100$. The background color represents the wave electric and magnetic fields acting on the electron, normalized to their maximum amplitudes. The relative size of the markers along the trajectory represents the changing γ-factor, while the color-coding represents the value of η.

therefore arrive at an important conclusion that most of the radiated emission during the direct laser acceleration occurs when the electron energy is relatively low.

The observed phase shift or phase mismatch between the γ-factor and the laser electric field E is characteristic of the direct laser acceleration. It necessarily reduces the value of η, as evident from equation (1). Since the laser electric and magnetic fields drop as the electron reaches its maximum energy, the energy increase cannot be efficiently utilized to increase the emitted power. Moreover, the counter-synchronism also suppresses emission of high energy photons. The maximum energy of emitted photons is limited by the electron energy, so the photons emitted near the turning points where most of the emissions occur would have the lowest energy of all the emitted photons.

While the counter-synchronism is a major downside of the direct laser acceleration, it can be successfully negated by introducing quasi-static plasma fields. At this stage, let us assume that the forward propagating laser pulse drives a longitudinal electron current that sustains a slowly-evolving azimuthal magnetic field coiled around the axis of the laser pulse. The details of the magnetic field generation will be carefully examined in the following section. In order to provide a simple estimate for the effect of this field on η, we set $\mathbf{E} = E\mathbf{e}_y$ and $\mathbf{B} = (B + B_*)\mathbf{e}_z$, where E and B are the fields of a plane wave, while B_* is the static plasma magnetic field.

We now assume that the plasma field B_* is so weak that its effect on the electron trajectory in the direct laser acceleration regime is negligible. We are looking for the threshold value of B_* where it begins to affect our estimates for η_{DLA}. Using expressions (7)–(9) for the electron momentum and its γ-factor, we find that

$$\eta \approx \frac{E}{E_S}\sqrt{1 + \kappa + \kappa^2}\,, \tag{13}$$

where for compactness we introduce a dimensionless quantity

$$\kappa \equiv \gamma B_*/E. \tag{14}$$

If $|\kappa|$ is small, then the expression (13) reduces to $\eta \approx \eta_{\mathrm{DLA}}$. However, the expression for η changes as $|\kappa|$ approaches unity. We can therefore set $|\kappa| \approx 1$ as the defining criterion for critical value $B_{*\mathrm{cr}}$. It is notable that according to these estimates the magnetic field of the plasma should increase η—and, as a result, the emission—even at amplitudes that are still well below the amplitude of the laser magnetic field:

$$B_{*\mathrm{cr}} \approx B/a_0^2 \ll B. \tag{15}$$

Here we once again take into account that in a plane wave the amplitudes of the electric and magnetic fields are the same, $E = B$, and that the γ-factor at highly-relativistic laser amplitudes scales approximately as $\gamma \approx a_0^2$.

Our estimates clearly indicate that even a plasma magnetic field of relatively moderate strength can significantly boost the photon emission during an electron's direct laser acceleration. If the required magnetic field can be generated by driving an intense laser pulse through a plasma, then this would make this concept a very promising method for creating significant numbers of high-energy photons with just a single laser pulse. Note that we assumed the energy gain by the electron remains unaffected by this plasma field, but it is plausible that this magnetic field can enhance the energy gain by changing the frequency of the transverse momentum oscillations. A somewhat similar effect has been observed for relatively weak transverse static plasma electric fields in laser-generated channels [27, 28], albeit at significantly lower intensities than the ones we are considering here.

3. Emission enhanced by plasma magnetic fields

The estimates presented in the previous section indicate that magnetic fields driven in a plasma can prove advantageous for the photon emission from laser-accelerated electrons. Motivated by these estimates, we here examine this scenario using fully self-consistent PIC simulations using the code EPOCH [29] in order to characterize the generated photon beam when using a laser pulse with parameters similar to the constructed Apollon laser in France. This permits us to explore the emission characteristics of electrons extending beyond the simple but illuminating regimes considered in section 2, which are observed in the physical system of interest.

It is intuitively clear that using a dense plasma would be beneficial for driving strong magnetic fields, because the current that sustains the field scales linearly with the plasma electron density. The laser can only drive such a current, though, as long as it can propagate through the plasma. At non-relativistic laser amplitudes, $a_0 \ll 1$, the cutoff electron density above which the plasma becomes opaque is determined only by the frequency of the incoming laser pulse through $n_{\mathrm{cr}} = m\omega^2/(4\pi e^2)$. This is often referred to as the classical critical density.

In contrast, a high-intensity laser pulse with $a_0 \gg 1$ can make an otherwise opaque plasma with a classically over-

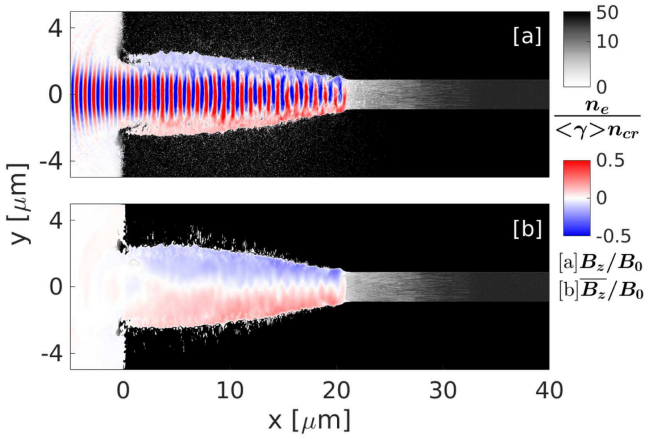

Figure 2. Snapshots taken at $t \approx 27$ fs of a structured target irradiated by a laser pulse with $a_0 \approx 257$. The gray-scale shows the relativistically adjusted electron density. The red and blue color-scale shows the z component of the magnetic field, the total field in the upper panel and the time-averaged field (over two laser cycles) in the lower panel.

critical electron density $n_e \gg n_{\rm cr}$ transparent. As the laser electric field accelerates plasma electrons to relativistic energies, it changes the optical properties of the plasma. A simplistic view is to treat this as an effective mass increase by a factor of $\langle\gamma\rangle$, where $\langle\gamma\rangle$ is the characteristic relativistic factor of the electron population. Even though this qualitative analogy to predict a γ factor enhancement of the critical density is helpful, it should be pointed out that it has limited applicability [30]. The effect described above has been termed as the relativistically induced transparency.

This phenomenon of relativistic transparency offers the attractive possibility of driving very strong plasma currents in classically over-critical plasmas with intense laser pulses. The plasma becomes opaque at $n_e/\langle\gamma\rangle \approx n_{\rm cr}$ and, taking into account that the γ-factor is driven by the laser to $\langle\gamma\rangle \approx a_0$, the relativistically adjusted critical density n_* can be estimated as $n_* \approx a_0 n_{\rm cr}$. Driving plasma currents in plasmas with n_e close to the relativistically adjusted critical density, however, presents a challenge, because the laser pulse propagation becomes extremely unstable.

Structured targets allow one to overcome the laser stability issues while taking full advantage of working with $n_e \gg n_{\rm cr}$ to generate strong magnetic fields [12]. The basic idea is to use a target with a channel that becomes relativistically transparent when irradiated by the laser pulse. The bulk of the target has a higher electron density than that in the channel, which allows for optical guiding of the laser pulse. The upper panel in figure 2 illustrates such guiding in a two-dimensional PIC simulation.

In the simulation whose results are shown in figure 2, we use a linearly-polarized 800 nm laser pulse with a peak intensity of 7×10^{22} W cm^{-2}, as mentioned before, similar to the Apollon facility. The pulse propagates in the positive direction along the x-axis with its electric field polarized in the plane of the simulation (the (x, y)-plane). The pulse is 90 fs long and has a focal spot of 1.1 μm (full-width at half maximum in regard to the intensity), focusing at normal incidence onto the entrance of the channel.

For simplicity, we use a target that consists only of electrons and protons. The bulk target density is $n_e = 100 n_{\rm cr}$, which makes it relativistically near-critical for the considered laser pulse with a peak normalized intensity of $a_0 \approx 257$. The channel electron density is set at $n_e = 10 n_{\rm cr}$. This choice was guided by target manufacturing considerations [31], as the availability of the materials and the techniques required for constructing the considered target are critical for the implementation of the discussed concept. The initial radius of the channel is $R = 0.9$ μm to provide good coupling of the laser energy into the channel. We use 20 macro-particles per cell to represent electrons and 20 macro-particles per cell to represent protons. The spatial resolution is 50 cells per μm along the x-axis and 100 cells per μm along the y-axis.

The change in optical properties of the plasma induced by the laser pulse is depicted in figure 2 by plotting the normalized relativistically adjusted electron density $n_e/\langle\gamma\rangle n_{\rm cr}$, where $\langle\gamma\rangle$ is the cell-averaged electron relativistic γ-factor. The channel becomes 'lighter' in the presence of the laser pulse, which signifies that it is optically transparent. The snapshots are taken at $t \approx 27$ fs, with $t = 0$ fs defined as the time when the laser pulse would reach its peak amplitude in the focal plane at $x = 0$ μm in the absence of the target.

In line with our expectations, the laser pulse drives a strong slowly-evolving magnetic field as it propagates along the relativistically transparent channel. As evident from the lower panel of figure 2, the amplitude of the time-averaged magnetic field is comparable to the instantaneous values dictated by the oscillating laser field. The averaging is performed over two laser cycles, and the field is normalized to $B_0 \approx 1.7$ MT, which is the peak amplitude of the magnetic field in the focal plane at $x = 0$ μm in the absence of the target. For reference, the similarly defined peak amplitude of the electric field is $E_0 \approx 5.13 \times 10^{14}$ V m^{-1}.

Also of note from this simulation is that the channel in figure 2 is significantly wider than it was prior to being irradiated by the pulse. This clearly indicates that there is non-negligible transverse ion movement, which then raises a question of the role that the ion mobility plays in the considered setup. In order to gain more insight, we have performed another simulation where the ions are immobile while all other parameters remain unchanged. Snapshots of the instantaneous and time-averaged magnetic fields from this simulation are shown in figure 3. Taking transverse lineouts at $x = 10$ μm, we find from figures 2 and 3 that the peak value of the time-averaged magnetic field decreases from roughly 0.75–0.5 MT by switching from immobile to mobile ions. The reduction in the case of mobile ions is possibly caused by the electron current being distributed over a larger channel cross-section. Nevertheless, the quasi-static magnetic field remains very strong and it has an unprecedented amplitude that is roughly 25% of the oscillating magnetic field in the laser pulse.

We can therefore conclude that the generation of a strong quasi-static magnetic field is a robust process with respect to the ion mobility. The situation is very different, however, for

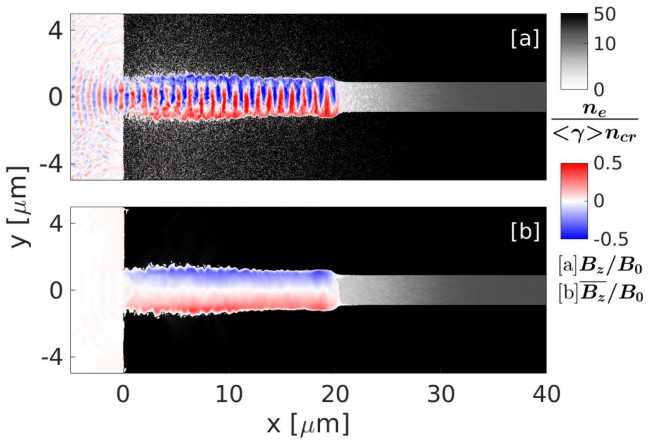

Figure 3. Snapshots taken at $t \approx 27$ fs of a structured target with immobile ions irradiated by a laser pulse with $a_0 \approx 257$. The gray-scale shows the relativistically adjusted electron density. The red and blue color-scale shows the z component of the magnetic field, the total field in the upper panel and the time-averaged field (over two laser cycles) in the lower panel.

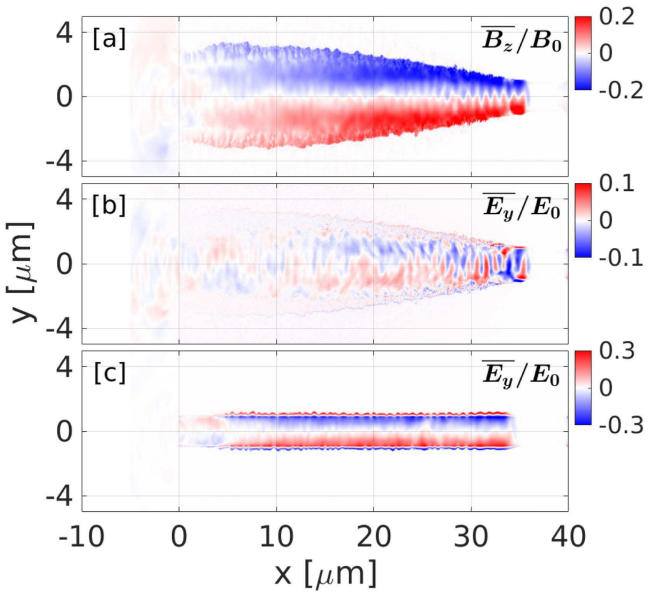

Figure 4. Snapshots of time-averaged electric and magnetic fields taken at $t \approx 107$ fs. The top two panels correspond to the simulation with mobile ions, while the lower panel corresponds to the simulation with immobile ions.

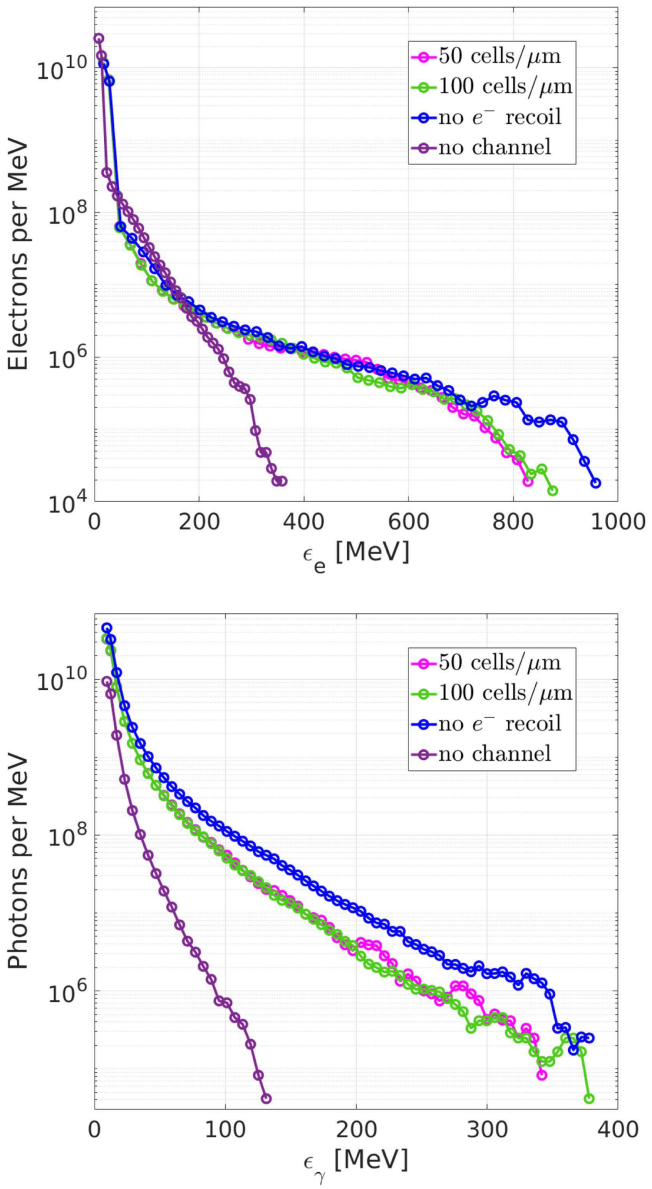

Figure 5. Snapshots of electron (top) and photon (bottom) energy spectra at $t = 107$ fs from simulations with and without the relativistically transparent channel ('no channel'). The runs with the channel were performed for two different resolutions: 50 and 100 cells per μm. In the 'no e^- recoil' run the radiation reaction is artificially turned off and the electrons emit photons without a recoil. The absolute numbers are calculated assuming a 1 μm width out of the plane of the 2D simulation.

quasi-static transverse electric fields that are also generated in the channel due to charge separation caused by the laser pulse. Figure 4 shows snapshots of the time-averaged transverse electric field $\overline{E}_y$ from the simulations with mobile (middle panel) and immobile (lower panel) ions. Clearly, the ion mobility dramatically reduces the electric field, as its peak value drops by more than an order of magnitude from $\overline{E}_y/E_0 \approx 0.3$ to $\overline{E}_y/E_0 \approx 0.03$ in the cross-section at $x = 20\ \mu$m.

It must be emphasized that in the case of immobile ions the relative strengths of the time-averaged electric field $\overline{E}_y$ and time-averaged magnetic field $\overline{B}_z$ are comparable: $\overline{B}_z/B_0 \sim \overline{E}_y/E_0$. In contrast to that, we have $\overline{B}_z/B_0 \gg \overline{E}_y/E_0$ if the ions are mobile. This feature is clearly noticeable when comparing the top two panels in figure 4. This result justifies our earlier focus on the slowly-evolving plasma magnetic field as the primary mechanism for enhancing the electron emission. From here onwards we restrict our discussion to the simulation with mobile ions.

We are primarily interested in high-energy electrons with $\gamma \gg a_0$ due to their potential to radiate multi-MeV photons. Figure 5 shows a snapshot of the electron spectrum generated by the laser pulse in the structured target. The laser pulse indeed generates an energetic electron tail with $\gamma \gg a_0$ or,

equivalently, $\epsilon_e \gg a_0 m_e c^2 \approx 125$ MeV. Maximum electron energies reach 800 MeV. The simulation was repeated using 100 cells per μm to verify that our results are not affected by the resolution, which can become a factor in PIC simulations of the direct laser acceleration [32].

For comparison to the channel geometry, an additional simulation was performed for a uniform target with an electron density of $100n_{cr}$. The target remains relativistically near-critical, so the laser propagation is significantly impeded. This negatively affects both the magnetic field generation and the electron acceleration, as we see that the corresponding electron spectrum shown in figure 5 has noticeably fewer energetic electrons compared to the simulation with the channel. This confirms the positive impact on electron acceleration of using a relativistically transparent channel which facilitates the development of an extended quasi-static magnetic field structure.

A direct way to quantify the impact of the plasma magnetic field on the emission is to examine the value of the parameter η for emitting electrons. The quantum-corrected emission process in our simulation is a discrete process in which individual photons are probabilistically emitted by accelerated electrons that simultaneously experience a recoil (radiation reaction). The corresponding emission algorithm implemented in EPOCH has been discussed in detail in [33]. We have recorded the data for all of the photon emissions during the simulation shown in figure 2 for post-processing, including the electric and magnetic fields acting on each electron during the timestep of emission. This information enables us to search deeper into the nature of the photon emissions.

We first reiterate that during the direct laser acceleration in a vacuum, the value of η drops with the increase of the γ-factor because of the counter-synchronism in oscillations of γ and of the laser electric field. In other words, high-energy electron emission is deemed to be inefficient in the absence of plasma fields (see section 2). Motivated by this observation, we now isolate the emissions by electrons with energies above 250 MeV during our simulation and further restrict the dataset to photon emissions with energies above 20 MeV. Remarkably, the parameter η reaches values as high as 0.2 (see figure 6), which validates our conjecture that the emission by energetic electrons becomes significantly more efficient in the presence of the plasma magnetic field.

The profound difference between the emission in a plasma channel and in a vacuum becomes more apparent when examining the local fields experienced by the selected electrons at their moments of emission. In figure 6 we present a scatterplot showing the perpendicular (to its instantaneous momentum) electric and magnetic fields for each electron when emitting, each value color-coded by the corresponding η of the particle. Here we observe that a significant number of emissions occur where there is a discrepancy between the local $E_\perp$ and $B_\perp$ field strengths. It is important to point out that the emissions further away from the central axis $E_\perp/E_0 = B_\perp/B_0$ show a higher value of η than the emissions on-axis where particles oscillating in vacuum would reside. These highest η values can be found at an offset of about

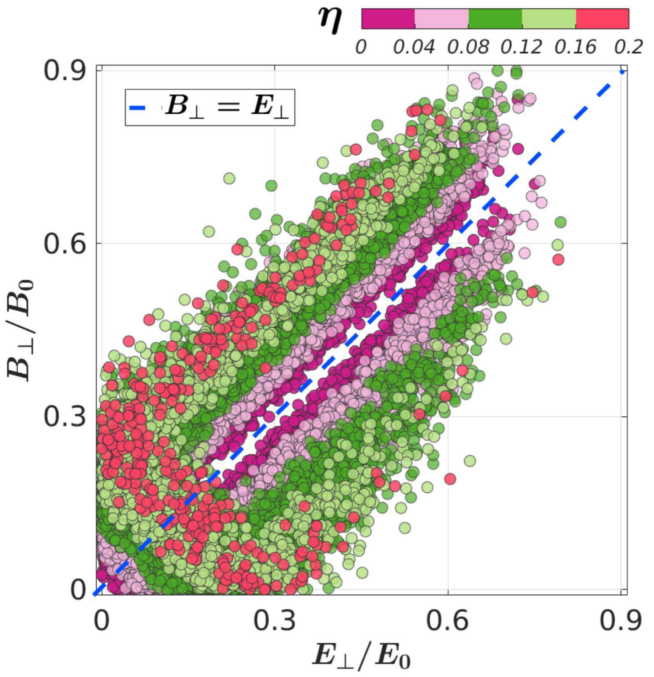

Figure 6. Scatterplot of emitting electrons in terms of the transverse electric and magnetic fields that they experience at the timestep of emission. Each circle represents an emission event, and they are color-coded by the characterizing η value. The data set was downsized by only selecting electrons with energies above 250 MeV that emit photons with energies above 20 MeV.

$B_\perp/(3B_0)$ from the central diagonal, which is roughly the strength of the magnetic field at the edge of the channel. Therefore, the strong plasma magnetic field generated by the laser-driven current can account for the elevated emission rates of the ultra-relativistic electrons that are observed in the simulations.

A snapshot of the resulting photon spectrum is shown in the lower panel of figure 5, where we also show the photon spectrum from the simulation without the channel. The range of the emitted photon energies and the overall number of multi-MeV photons is dramatically increased with the introduction of the channel sustaining the extended quasi-static magnetic field. The emission rate is increased so much that the electron recoil caused by the photon emission starts to impact the electron dynamics. In order to demonstrate this, we turn the electron recoil off and repeat the same simulation. Only the most energetic tail of the electron spectrum is visibly impacted, but the changes in the electron spectrum are sufficient to significantly alter the entire photon spectrum (see lower panel of figure 5). Without accounting for the electron recoil, we generate 3.86×10^{12} multi-MeV photons. Incorporating radiation reaction reduces this number to 1.69×10^{12}, but this number is still an order of magnitude higher than what we find in a simulation without a channel where the total number of multi-MeV photons is only 1.77×10^{11}.

This enhancement of the emission from high energy electrons in strong magnetic fields has the additional benefit of corresponding with strongly collimated emission. Since the opening cone of the emission angle is inversely proportional

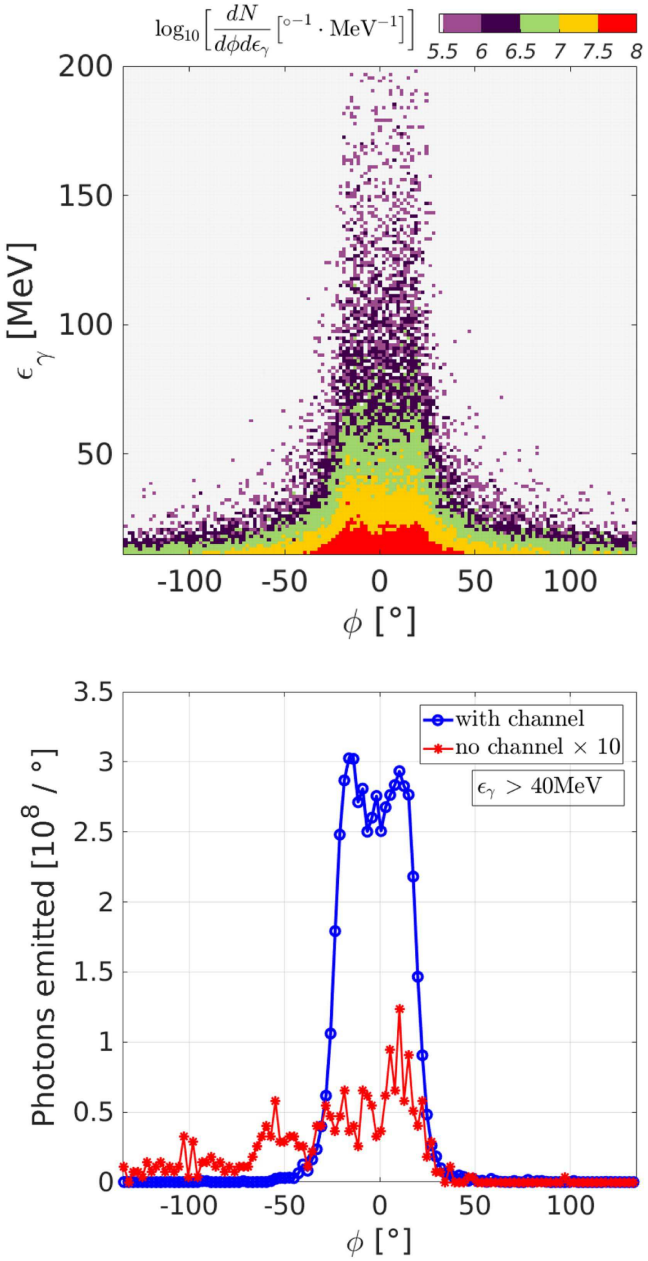

Figure 7. Angular distribution of the photons emitted in targets with (blue) and without (red) a channel that are irradiated by a laser pulse with $a_0 \approx 257$ as shown in figure 2. These are all of the emissions that have occurred by $t \approx 107$ fs. A large number of high energy photons is emitted forward into an opening angle of $\pm 30°$ in the structured target simulation.

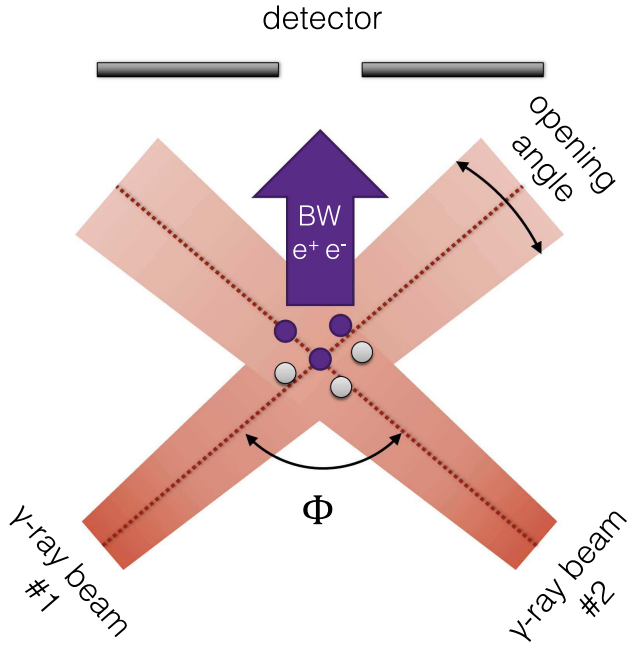

Figure 8. Schematic setup for pair production via two-photon collisions by employing two γ-ray beams.

to the Lorentz-factor of the emitting electron, $\Delta\alpha \sim 1/\gamma$, an ultra-relativistic electron will essentially emit parallel to its momentum. In our regime, the momentum of the accelerated electrons is primarily directed forward. Figure 7 plots the angular distribution (with respect to the laser propagation direction) of the emitted photons (calculated from their x and y momenta) across the observed energy range, showing that the emission of the highest energy photons is limited to a range of approximately $\pm 30°$ in the channel geometry. These photon yields are calculated by assuming that the generated beam of photons from the 2D simulation has a transverse (out-of-plane in the z-direction) dimension of 1 μm, comparable with the focal spot size. As the magnetic field can tightly constrain the electron motion in the channel [12], this narrow angular spread is expected. For comparison, we also plot the angular distribution from the simulation without a channel in figure 7 and observe emission that is more diffuse and at much lower levels. It is the combination of the enhanced gamma-ray production and the high degree of collimation, both facilitated by the quasi-static magnetic field, that opens up exciting avenues of application for gamma-ray sources. In the next section we demonstrate how this technique can be exploited for one such prospect.

4. Pair production via photon–photon collisions

In section 3, we demonstrated how relativistic transparency and strong quasi-static magnetic fields can be leveraged to generate a well-directed beam of energetic photons (gamma-rays). The directivity of the beam opens up the exciting possibility of colliding two such beams away from the target in a vacuum to generate electron–positron pairs through a linear Breit–Wheeler process [14]. The corresponding setup is schematically shown in figure 8.

As already mentioned in the introduction, the linear Breit–Wheeler process plays a fundamental role in astrophysical phenomena, but it has not yet been directly observed in laboratory conditions. The cross-section for pair production by two photons with energies ϵ_{γ_1} and ϵ_{γ_2} colliding at an angle

Φ is given by [34]

$$\sigma_{\gamma\gamma} = \frac{\pi}{2} r_e^2 (1 - \zeta^2) \left[-2\zeta(2 - \zeta^2) + (3 - \zeta^4) \ln \frac{1 + \zeta}{1 - \zeta} \right], \tag{16}$$

where $r_e \approx 2.8 \times 10^{-15}$ m is the classical electron radius and $\zeta \equiv \sqrt{1 - 1/s}$, with

$$s = \frac{\epsilon_{\gamma_1} \epsilon_{\gamma_2}}{2 m_e^2 c^4} (1 - \cos \Phi). \tag{17}$$

This cross-section has a threshold, $s > 1$, dictated by the energy conservation, which translates into the following requirement for the energies of colliding photons:

$$\epsilon_{\gamma 1} \epsilon_{\gamma 2} > \frac{2 m_e^2 c^4}{1 - \cos \Phi}. \tag{18}$$

In order to recreate the necessary conditions for observing this process, not only high photon densities, but also high photon energies are required.

Two different approaches have been proposed that rely on high-power lasers for overcoming these challenges. One approach is to fire a gamma-ray beam into the high-temperature radiation field of a laser-heated hohlraum [35], whereas the other approach is to actually collide two gamma-ray beams [36, 37]. In what follows, we explore the second approach of using two gamma-ray beams, each like the one obtained from the PIC simulation in the previous section of the paper. These beams are particularly suited for this approach, since they have a large concentration of energetic photons [12].

In order to provide an upper estimate for the number of pairs that can be produced, we consider the most optimistic case of two gamma-ray beams colliding head-on before they significantly expand. In this case, the number of collisions experienced by a single photon as it goes through an oncoming beam is $N_{\rm coll} \approx N_\gamma \sigma_{\gamma\gamma}/S$, where $N_\gamma \approx 10^{12}$ is the number of multi-MeV gamma-rays in each beam and $S \approx 1\ \mu\text{m}^2$ is the beam cross-section. Even for the cross-section of $\sigma_{\gamma\gamma} \approx \pi r_e^2 \approx 2.5 \times 10^{-29}$ m^2 there is on average less than one collision event, $N_{\rm coll} \approx 2.5 \times 10^{-5}$. The total number of pairs is simply $N_{\rm pairs} \approx N_\gamma N_{\rm coll}$, so we have the following estimate for the maximum number of pairs that can be produced:

$$N_{\rm pairs}^{\rm max} \approx N_\gamma^2 \sigma_{\gamma\gamma}/S \approx 2.5 \times 10^7. \tag{19}$$

Such a high number of pairs is a direct consequence of the unprecedented number of collimated multi-MeV photons that a structured target with a quasi-static magnetic field can generate.

In the setup shown in figure 8, the number of generated pairs would be significantly reduced because of the beam divergence and because the two beams collide at an angle instead of colliding head-on. However, the high number given by equation (19) suggests that a large number of pairs can still be generated. We consider two scenarios where the two beams collide at an angle of $\Phi = 15°$ and at an angle of $\Phi = 90°$. In both cases, the collisions occur roughly 5 mm away from the laser-irradiated targets that produced the gamma-ray beams. The collision location is deliberately removed from the original targets in order to reduce possible interference from particles and photons other than the gamma-rays of interest. In order to make the calculation manageable, we only consider photons that were emitted into a limited opening angle (from $\pm 3°$ to $\pm 10°$). Our goal is to evaluate the pair production rate under such restrictive conditions, which can pave the way for designing experimental setups in the future.

In the case of the $\Phi = 15°$ collision angle, only photons that satisfy the condition

$$\frac{\epsilon_{\gamma 1} \epsilon_{\gamma 2}}{m_e^2 c^4} > 59 \tag{20}$$

will contribute to the pair-creation. This condition follows directly from equation (18). The cross-section peaks at

$$\frac{\epsilon_{\gamma 1} \epsilon_{\gamma 2}}{m_e^2 c^4} \approx 100 \tag{21}$$

with a value of

$$\sigma_{\gamma\gamma}^{\rm max} \approx 0.75 \pi r_e^2 \tag{22}$$

and then slowly decreases for higher values of $\epsilon_{\gamma 1} \epsilon_{\gamma 2}$. These estimates indicate that multi-MeV photons will be the major contributors to the pair-production. It is worth pointing out that the photon numbers produced by the source considered in section 3 dramatically increase as we decrease the photon energies. Guided by these considerations and the intention of making the pair production simulation feasible, we retain only photons with energies above 1 MeV in the two beams.

Simulating the photon–photon collisions in two colliding photon beams presents a serious computational challenge. Even after applying the criteria described above, we are left with over 10^5 macro-particles representing the photon spectrum shown in figure 7. This would then require at least 10^{10} binary collision tests in order to check for all of the macro-particles whether or not collisions have occurred. Even for the simplest collision tests, this would lead to unacceptable computation times.

In order to overcome this difficulty, we use the TrI-LEns code [38] that was specifically designed for swift collision detection amongst large numbers of particles. Unlike a PIC code, TrI-LEns does not use a mesh of cells; particles move freely in space and are managed in a tree-hierarchy. To dramatically reduce the number of binary collision tests, TrI-LEns uses a modern collision detection algorithm based on bounding volumes that operates with little computational effort and without sacrificing accuracy.

We initialize the photon collision simulation by importing photon macro-particle data generated during the PIC simulation. In TrI-LEns, each macro-particle is interpreted as a rectangular prism (hereafter 'box') uniformly filled with photons. To translate the PIC data to this format, we uniformly subdivide each cell defined in the PIC code by the number of macro-particles assigned to each cell to make one box for each macroparticle. In order to perform a 3D simulation, we assign to each box a height of 1 μm, which is

roughly the transverse size of the channel in which the photons are generated. The subdivision is only performed in the plane of the PIC simulation, and all photons in one box have the same momentum as the original macro-particle. The described procedure of distributing photons in space is essential to provide the necessary input for the collision detection in the simulation.

Once the photon boxes have been initialized in space with their appropriate densities and momenta, TrI-LEns can evolve their motion forward in time to check for collisions. Time steps consist of testing for collisions and then pushing the virtual photon boxes. The code currently does not involve any propagating fields and has no mesh, so there is no stability condition that typically severely limits the time step in PIC simulations. This allows for a significant speed up of our calculations. The only aspect that is impacted by the time-step is the chronological order of the collisions. Even with this code, it is computationally demanding to recover the exact chronological order of all of the photon collisions [38].

The collision algorithm implemented in TrI-LEns first checks for the overlap between the rectangular boxes filled with photons. Once an overlap is detected between two boxes, the code calculates an actual interaction volume between the photons. It then uses the cross-section given by equation (16) and the interaction volume to calculate how many electron–positron pairs are produced in total by the colliding photons from the two boxes. Note that the cross-section is the same for all of the collisions in one such event, because all photons in one box have the same momentum.

An electron and a positron are emitted from each of these pair production events as two macro-particles. The emission is calculated in a frame of reference where the two boxes of photons collide head-on. The direction of emission in this frame of reference is isotropic and it is therefore chosen randomly, but the momenta of the emitted macro-particles are constrained by the energy and momenta conservation requirements. Note that the angular distribution of the emitted pairs is no longer isotropic when transformed back to the laboratory frame of reference if the photon boxes collide at an angle. Once two boxes of photons have collided, the code reduces the number of photons in each box by the number of emitted electron–positron pairs to account for the photon annihilation. The photons are again assumed to be uniformly distributed, so the code effectively reduces the photon density in each box. The pair creation in our algorithm has a threshold, with a pair being produced in a collision of two virtual boxes only if the calculated number is greater than unity.

Figure 9 shows the positron yields from the collisions between two gamma-ray beams that we simulated. The opening angle of the simulated photons is $\pm 3^\circ$ from the laser axis for each beam. The upper panel is for a $\Phi = 90^\circ$ collision between the beams that produces a total of 1153 positrons, whereas the lower panel is for a $\Phi = 15^\circ$ collision that results in 173 positrons. All incoming photons are moving in the (x, y)-plane shown with color in both panels. In these scatter plots, the markers are macro-particles representing generated positrons. Since the events are relatively rare, one macro-particle roughly corresponds to one positron.

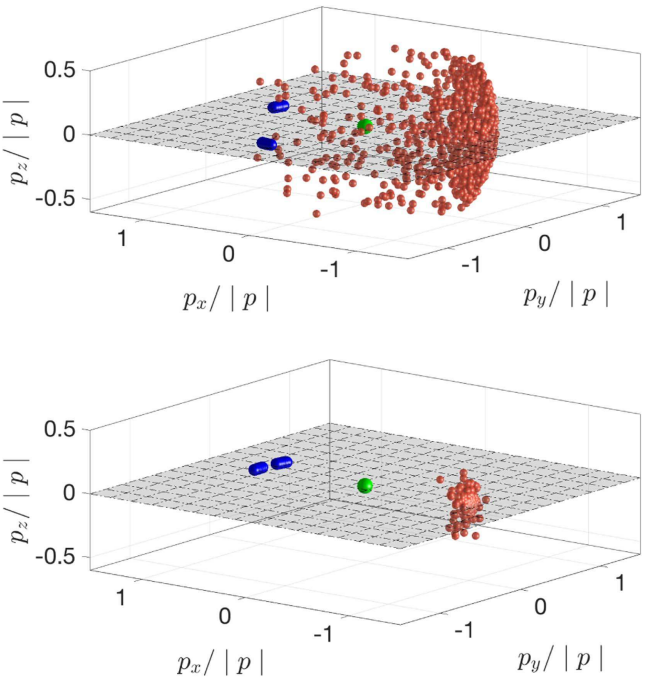

Figure 9. Scatterplot of positrons (represented by macro-particles) based on the direction of their momentum. The blue markers represent photons in the incoming gamma-ray beams, with the momentum inverted (with respect to the origin shown by a green marker) to prevent an overlap with positron markers. The collision angles for the beams are $\Phi = 90^\circ$ (upper) and $\Phi = 15^\circ$ (lower).

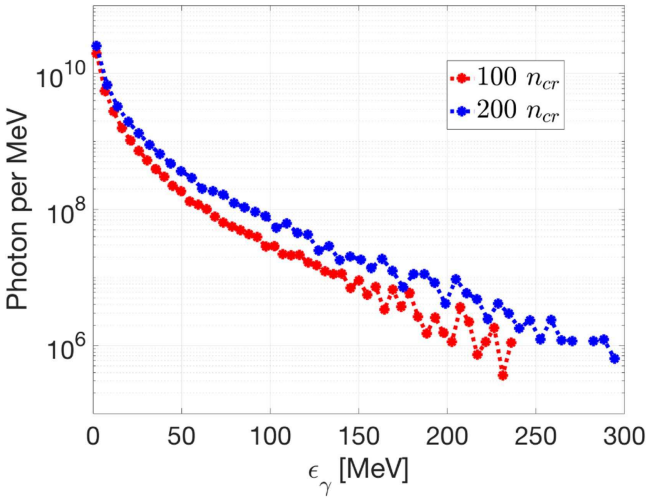

Figure 10. Energy distribution of photons in the two colliding photon beams prior to the collision. The upper curve is generated by a source with a bulk target density of $n_e = 200 n_{\mathrm{cr}}$. The lower curve is generated by a source with a bulk target density of $n_e = 100 n_{\mathrm{cr}}$. The corresponding angle resolved distribution is shown in figure 7.

It must be pointed out that two different photon sources are required to simulate the collision. Taking two identical sources would cause for an artificially high number of photons to collide, which is a geometrical effect. Instead of introducing additional randomization, we decided to use two

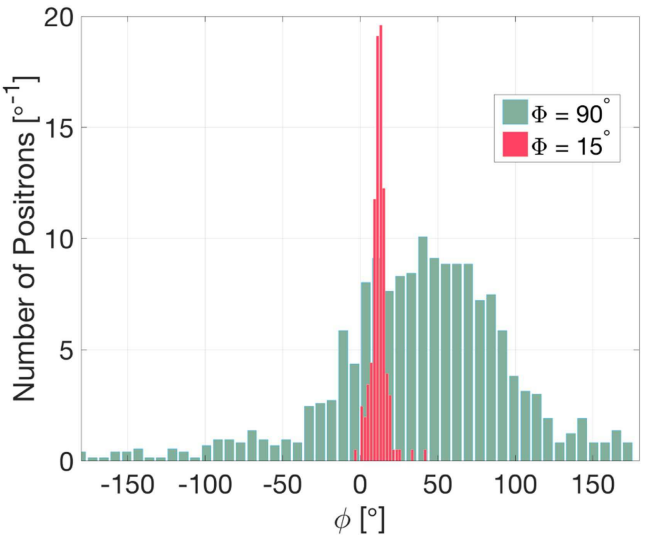

Figure 11. Histogram of the azimuthal angle ϕ representing the direction of the positron momentum in the plane of the colliding photon beams. The narrow distribution is for $\Phi = 15°$ (red) and the wider distribution is for $\Phi = 90°$ (green).

sources that were produced by targets with different bulk densities. One source is from the exact setup described in the previous section that had a bulk density of $n_e = 100n_{\rm cr}$. The second source was instead calculated using a bulk density of $n_e = 200n_{\rm cr}$ but with the same parameters for the laser pulse. The photon spectra that were used for the photon collision simulations are shown in figure 10.

The difference in the photon spectra causes the emitted positron beam to be slightly asymmetric. Angular distributions of the positrons in the plane of the colliding photon beams are plotted in figure 11 for the two collision angles that we have considered. The colliding photon beams are centered around $\phi = 0°$, so the resulting positron beams would be symmetric for photon beams with the same energy distribution.

It is evident from figure 7 that a structured target generates a gamma-ray beam that has somewhat more photons off-axis, with the maxima at about $\pm 15°$. In order to further explore the parameter space, we have performed additional simulations where these maxima were collided at $\Phi = 15°$ instead of using the central parts of the beams as we have done so far. This was achieved by re-orienting the colliding beams by rotating them by 15° with respect to their original orientations. The simulations were performed by selecting photons emitted into an opening angle of $\pm 3°$, $\pm\ 6°$, and $\pm 10°$ around the selected maximum in each beam. The resulting yields are 188, 226, and 673 pairs. Not surprisingly, the number of generated pairs for the $\pm 3°$ opening angle has now increased compared to the previous simulations that used the central parts of the photon beams. Moreover, as the yield increases with the opening angle, so does the divergence of the produced positrons. This provides an opportunity for a trade-off between the divergence and the yield that can further be exploited in designing an experimental setup.

We can then conclude that, despite the fact that the interaction region is significantly removed from the laser-irradiated targets that generate the photons, we are able to generate on the order of 10^3 pairs. The collimation of the generated positrons can be improved by reducing the collision angle, as clearly shown in the lower panel of figure 9. However, improved collimation comes at the expense of the positron yield. It remains to be determined whether such a trade-off is beneficial in the context of the schematic setup shown in figure 8.

5. Summary and conclusions

We have examined the role of a plasma magnetic field driven in a classically over-critical plasma by a high-intensity laser pulse. Specifically, PIC simulations demonstrate the potential of such setups to exploit the phenomenon of relativistic transparency, which enables a laser-driven current capable of generating magnetic fields of unprecedented strength. This magnetic field, in turn, is shown to significantly enhance the emission rates of ultra-relativistic electrons traversing the field. An analysis of various kinds of electron motion in a laser field, including the direct laser acceleration mechanism, highlight the non-trivial change that a background magnetic field induces in electron motion and radiation rates. PIC simulations corroborate this analysis by showing that a classically over-critical (but relativistically transparent) channel embedded in a relativistically near-critical bulk target facilitates the emission of large quantities of multi-MeV gamma-rays into an angular cone, promoted by the large magnetic field at the channel edges.

A host of potential applications arises from this type of gamma-ray generation capability, but we focused here on the exciting prospect of observing the linear Breit–Wheeler process of pair production. By colliding two such dense, collimated gamma-ray beams that can be created through our laser-target setup, the TrI-LEns tree code demonstrates positron production of varying yield (up to $\sim 10^3$) and directionality based on the angle of incidence. In contrast to the previous work on the topic [36, 37], we used an exact photon beam calculated in a PIC simulation to make quantitative predictions regarding the positron yield and directivity. Evidently, this technique of gamma-ray production opens a new door into fundamental physics research and gamma-ray applications that can be realized with today's technology.

Acknowledgments

This research was supported by the National Science Foundation under Grant No. 1632777 and the US Air Force project AFOSR No. FA9550-17-1-0382. Simulations were performed using the EPOCH code (developed under UK EPSRC Grants No. EP/G054940/1, No. EP/G055165/1, and No. EP/G056803/1) using HPC resources provided by the TACC at the University of Texas and the Comet cluster at the SDSC at the University of California at San Diego. This work used the Extreme Science and Engineering Discovery Environment

(XSEDE), which is supported by National Science Foundation grant number ACI-1548562.

ORCID iDs

O Jansen https://orcid.org/0000-0003-2220-9342
A V Arefiev https://orcid.org/0000-0002-0597-0976

References

[1] Aléonard M *et al* 2011 *WHITEBOOK ELI – Extreme Light Infrastructure; Science and Technology with Ultra-Intense Lasers* (https://doi.org/10.13140/2.1.1227.0889)
[2] https://polytechnique.edu/en/content/birth-apollonmost-powerful-laser-worldwide
[3] Chriaux G *et al* 2012 Apollon-10p: Status and implementation *AIP Conf. Proc.* **1462** 78–83
[4] Schlenvoigt H-P *et al* 2008 A compact synchrotron radiation source driven by a laser-plasma wakefield accelerator *Nat. Phys.* **4** 130–3
[5] Vranic M, Martins J L, Vieira J, Fonseca R A and Silva L O 2014 All-optical radiation reaction at 10^{21} W cm^{-2} *Phys. Rev. Lett.* **113** 134801
[6] Mackenroth F, Neitz N and Di Piazza A 2013 Novel aspects of radiation reaction in the ultrarelativistic quantum regime *Plasma Phys. Control. Fusion* **55** 124018
[7] Gonoskov A, Bastrakov S, Efimenko E, Ilderton A, Marklund M, Meyerov I, Muraviev A, Sergeev A, Surmin I and Wallin E 2015 Extended particle-in-cell schemes for physics in ultrastrong laser fields: review and developments *Phys. Rev.* E **92** 023305
[8] Ridgers C P, Brady C S, Duclous R, Kirk J G, Bennett K, Arber T D, Robinson A P L and Bell A R 2012 Dense electron–positron plasmas and ultraintense γ rays from laser-irradiated solids *Phys. Rev. Lett.* **108** 165006
[9] Nakamura T, Koga J K, Esirkepov T Z, Kando M, Korn G and Bulanov S V 2012 High-power γ-ray flash generation in ultraintense laser-plasma interactions *Phys. Rev. Lett.* **108** 195001
[10] Capdessus R, d'Humières E and Tikhonchuk V T 2013 Influence of ion mass on laser-energy absorption and synchrotron radiation at ultrahigh laser intensities *Phys. Rev. Lett.* **110** 215003
[11] Ji L L, Pukhov A, Nerush E N, Kostyukov I Y, Akli K U and Shen B F 2014 Near QED regime of laser interaction with overdense plasmas *Eur. Phys. J. Spec. Top.* **223** 1069–82
[12] Stark D J, Toncian T and Arefiev A V 2016 Enhanced multi-MeV photon emission by a laser-driven electron beam in a self-generated magnetic field *Phys. Rev. Lett.* **116** 185003
[13] Malka V, Faure J, Gauduel Y A, Lefebvre E, Rousse A and Phuoc K T 2008 Principles and applications of compact laser-plasma accelerators *Nat. Phys.* **4** 1626–9
[14] Breit G and Wheeler J A 1934 Collision of two light quanta *Phys. Rev.* **46** 1087–91
[15] Piran T 2005 The physics of gamma-ray bursts *Rev. Mod. Phys.* **76** 1143–210
[16] Ruffini R, Vereshchagin G and Xue S-S 2010 Electron–positron pairs in physics and astrophysics: from heavy nuclei to black holes *Phys. Rep.* **487** 1–140
[17] Nikishov A I 1962 Absorption of high-energy photons in the Universe *J. Exp. Theor. Phys.* **14** 393–4 (http://jetp.ac.ru/cgi-bin/dn/e_014_02_0393.pdf)
[18] Burke D L *et al* 1997 Positron production in multiphoton light-by-light scattering *Phys. Rev. Lett.* **79** 1626–9
[19] Landau L D and Lifshitz E M 1971 *The Classical Theory of Fields* (Oxford: Pergamon)
[20] Ridgers C P, Kirk J G, Duclous R, Blackburn T G, Brady C S, Bennett K, Arber T D and Bell A R 2014 Modelling gamma-ray photon emission and pair production in high-intensity lasermatter interactions *J. Comput. Phys.* **260** (Suppl. C) 273–85
[21] Narozhnyi N B and Fofanov M S 1996 Photon emission by an electron in a collision with a short focused laser pulse *J. Exp. Theor. Phys.* **35** 35079708 (http://jetp.ac.ru/cgi-bin/dn/e_083_01_0014.pdf)
[22] Phuoc K T, Corde S, Thaury C, Malka V, Tafzi A, Goddet J P, Shah R C, Sebban S and Rousse A 2012 All-optical compton gamma-ray source *Nat. Photon.* **6** 308–11
[23] Cole J M *et al* 2018 Experimental evidence of radiation reaction in the collision of a high-intensity laser pulse with a laser-wakefield accelerated electron beam *Phys. Rev.* X **8** 011020
[24] Robinson A P L, Arefiev A V and Neely D 2013 Generating 'superponderomotive' electrons due to a non-wake-field interaction between a laser pulse and a longitudinal electric field *Phys. Rev. Lett.* **111** 065002
[25] Arefiev A V, Robinson A P L and Khudik V N 2015 Novel aspects of direct laser acceleration of relativistic electrons *J. Plasma Phys.* **81** 475810404
[26] Arefiev A V, Khudik V N, Robinson A P L, Shvets G, Willingale L and Schollmeier M 2016 Beyond the ponderomotive limit: direct laser acceleration of relativistic electrons in sub-critical plasmas *Phys. Plasmas* **23** 056704
[27] Khudik V, Arefiev A V, Zhang X and Shvets G 2016 Universal scalings for laser acceleration of electrons in ion channels *Phys. Plasmas* **23** 103108
[28] Arefiev A V, Breizman B N, Schollmeier M and Khudik V N 2012 Parametric amplification of laser-driven electron acceleration in underdense plasma *Phys. Rev. Lett.* **108** 145004
[29] Arber T D *et al* 2015 Contemporary particle-in-cell approach to laser-plasma modelling *Plasma Phys. Control. Fusion* **57** 113001
[30] Stark D J, Bhattacharjee C, Arefiev A V, Toncian T, Hazeltine R D and Mahajan S M 2015 Relativistic plasma polarizer: impact of temperature anisotropy on relativistic transparency *Phys. Rev. Lett.* **115** 025002
[31] Wei M, Williams J and Arefiev A 2017 private communication at General Atomics
[32] Arefiev A V, Cochran G E, Schumacher D W, Robinson A P L and Chen G 2015 Temporal resolution criterion for correctly simulating relativistic electron motion in a high-intensity laser field *Phys. Plasmas* **22** 013103
[33] Arber T D *et al* 2015 Contemporary particle-in-cell approach to laser-plasma modelling *Plasma Phys. Control. Fusion* **57** 113001
[34] Beresteskii V B, Lifshitz E M and Pitaevskii L P 1982 *Quantum Electrodynamics* (Oxford: Butterworth-Heinemann)
[35] Pike O J, Mackenroth F, Hill E G and Rose S J 2014 A photon–photon collider in a vacuum hohlraum *Nat. Photon.* **8** 434–6
[36] Ribeyre X, d'Humières E, Jansen O, Jequier S, Tikhonchuk V T and Lobet M 2016 Pair creation in collision of γ-ray beams produced with high-intensity lasers *Phys. Rev.* E **93** 013201
[37] Ribeyre X, d'Humires E, Jansen O, Jequier S and Tikhonchuk V T 2017 Electron–positron pairs beaming in the Breit–Wheeler process *Plasma Phys. Control. Fusion* **59** 014024
[38] Jansen O, d'Humires E, Ribeyre X, Jequier S and Tikhonchuk V T 2018 Tree code for collision detection of

large numbers of particles applied to the Breit–Wheeler process *J. Comput. Phys.* **355** (Suppl. C) 582–96